The Astrophysical Journal, 958:43 (11pp), 2023 November 20 https://doi.org/10.3847/1538-4357/ad01b6

Improving Coronal Hole Detections and Open Flux Estimates

Ronald M. Caplan, Emily I. Mason, Cooper Downs, and Jon A. Linker
Predictive Science Inc., 9990 Mesa Rim Road, Suite 170, San Diego, CA 92121, USA; caplanr@predsci.com
Received 2023 May 22; revised 2023 September 29; accepted 2023 October 7; published 2023 November 10

Abstract

One systematic limitation of solar coronal hole (CH) detection at extreme ultraviolet (EUV) wavelengths is the obscuration of dark regions of the corona by brighter structures along the line of sight. Another problem arises when using CHs to compute the Sun's open magnetic flux, where surface measurements of the radial magnetic field, $B_r^{\odot}$, are situated slightly below the effective height of coronal EUV emission. In this paper, we explore these two limitations utilizing a thermodynamic magnetohydrodynamic (MHD) model of the corona for Carrington rotation (CR) 2101, where we generate CH detections from EUV 193 Å images of the corona forward-modeled from the MHD solution, and where the modeled open field is known. We demonstrate a method to combine EUV images into a full Sun map that helps alleviate CH obscuration called the *minimum intensity disk merge* (MIDM). We also show the variation in measured open flux and CH area that is due to the effective height differences between EUV and $B_r^{\odot}$ measurements. We then apply the MIDM method to SDO/AIA 193 Å observations from CR 2101, and conduct an analogous analysis. In this case, the MIDM method uses time-varying images, the effects of which are discussed. We show that overall, the MIDM method and an appreciation of the effective height mismatch provide a useful new way to extract a broader view of CHs, especially near the poles. In turn, they enable improved estimates of the open magnetic flux, and help facilitate comparisons between models and observations.

Unified Astronomy Thesaurus concepts: Solar corona (1483); Solar coronal holes (1484); Solar surface (1527); Astronomy software (1855); Astronomy data analysis (1858)

1. Introduction

Coronal holes (CHs) appear as regions of relatively low intensity in extreme ultraviolet (EUV) and X-ray images (or bright regions in He I 10830 absorption; Sheeley et al. 1976; Bohlin 1977; Harvey & Sheeley 1977). They are a key component of coronal structure, and are inextricably tied to the origin of the solar wind. They are the source of fast solar wind streams (Krieger et al. 1973), which in turn lead to recurrent geomagnetic activity (Neupert & Pizzo 1974). They are also recognized as playing an important role in the genesis of the slow solar wind. In quasi-static theories, the slow wind arises from regions of large expansion factor near the boundaries (Wang & Sheeley 1990; Cranmer et al. 2007). Dynamic theories of the slow wind require reconnection between open- and closed-field regions, known as interchange reconnection (Fisk et al. 1998; Crooker et al. 2002; Antiochos et al. 2011); the imprints of such reconnection have been reported in periodic density structures and highly variable first ionization potential bias measurements throughout the slow wind (Schwadron et al. 1999; Viall & Vourlidas 2015), and low-coronal signatures of interchange reconnection at CH boundaries have recently been investigated via boundary complexity analysis (Mason & Uritsky 2022).

CHs have long been known to be associated with open magnetic fields (Altschuler et al. 1972). Along these open magnetic field lines, the density and temperature of the outflowing solar wind plasma fall rapidly with height, leading to the paucity of EUV and X-ray emission that is observed in CHs. Open magnetic flux from CHs is therefore expected to be the dominant source of the magnetic field in the heliosphere. Full-Sun detections of CHs can be used to estimate the open magnetic flux by overlaying them on photospheric magnetic field measurements.

Given the crucial role played by CHs and their boundaries, several methods for automatic or semiautomatic detection have appeared (Henney & Harvey 2005; Scholl & Habbal 2008; Kirk et al. 2009; Krista & Gallagher 2009; Rotter et al. 2012; Lowder et al. 2014; Verbeeck et al. 2014; Boucheron et al. 2016; Caplan et al. 2016; Garton et al. 2018; Heinemann et al. 2019). However, accurately identifying the CH boundaries over the whole Sun remains challenging due to many factors. Routine measurements of the Sun are generally only available along the Sun–Earth line, with the exception of additional viewing angles from the Solar Terrestrial RElations Observatory (STEREO; Kaiser 2005) and Solar Orbiter spacecraft (Müller et al. 2020). Obscuration by nearby bright coronal structures, the ambiguity created by line-of-sight (LOS) integration, and the inherent assumptions of any given detection algorithm all introduce uncertainties in the quantification of CH regions. Quantitative differences between magnetic maps from different observatories (e.g., Riley et al. 2014) further complicate the estimation of open magnetic flux. While comparisons of CH detection methods have recently been performed (Linker et al. 2021; Reiss et al. 2021), it is clear there is no *ground truth* open field data to which full-Sun EUV CH observations can be compared. Estimates of open magnetic flux utilizing full-Sun CH maps have consistently led to a significant underestimate when compared to the open flux measured at 1 au (Linker et al. 2017; Lowder et al. 2017; Wallace et al. 2019), one aspect of what is commonly called the *open flux problem* (Linker et al. 2017).

In this paper, we identify sources of systematic error in CH detection that arise from the LOS-integrated nature of EUV images. Specifically, we explore the issues of obscuration of CHs by nearby bright material, and the mismatch of effective

heights of EUV and magnetic field measurements. We describe a strategy for limiting CH obscuration, called minimum intensity disk merge (MIDM; Caplan et al. 2016; Linker et al. 2021). It is an alternative method to traditional synoptic mapping to combine multiple full-disk EUV images into a single full Sun map. To demonstrate issues with obscuration, we focus on the time period of Carrington rotation (CR) 2101 (2010 September 5 to 2010 October 3), the same one studied in Linker et al. (2021). As in Linker et al. (2021), we employ a thermodynamic MHD simulation of this time period to explore detection issues in a model where the true quantities (such as open flux) are known. The thermodynamic MHD approach extends the domain to $30\,R_\odot$, where outflows are typically super-Alfvénic, and allows the plasma density and temperature to be computed with sufficient accuracy to forward model EUV and soft X-ray emission and other remote sensing observables (Lionello et al. 2009; Downs et al. 2010, 2013). We refer to the forward-modeled emission as synthetic emission.

The paper is outlined as follows: Section 2 describes CH obscuration and the details of the MIDM procedure, while Section 3 presents the results of applying MIDM to a simulation, where the open field is known and the process can be effectively evaluated. We also discuss the effects of various *effective heights* when extrapolating magnetic field data. We then apply the MIDM method to actual EUV observations in the subsequent section. The final section discusses the implications of this method and how it can be used to improve both model and observational analyses in the future.

2. CH Obscuration and the MIDM Procedure

Many sources (e.g., DeForest 2004; Gibson et al. 2010; Downs et al. 2021) have documented the geometric distortions and lower fidelity data inherent in observing along oblique LOS (those deviating away from the disk center and looking toward the limbs). The main challenge that generates CH obscuration is illustrated in Figure 1. When closed loops (with correspondingly high emission, depicted in blue) are located adjacent to lower-emission open field (red), an observer located along the black-dashed LOS must look at the open/closed boundary through the bright plasma. They would therefore derive a boundary that was farther from the loop, resulting in an underestimation of the region's open flux. An analogous observer located along an LOS that does not intersect the coronal loops would see the true open/closed boundary with greater accuracy, and would define a larger CH. In order to address this issue, we have formulated the MIDM method. The basic idea of this method is to combine multiple EUV disk images from various vantage points, retaining the minimum emission in any overlapping regions, in order to emphasize the extent of CHs.

The MIDM procedure can be described as follows: an empty full Sun map is created. The EUV images that will be used are projected into a latitude/longitude map in Carrington coordinates, and each pixel is assessed before being used to populate the full Sun map. Naturally, many pixels will have data from multiple EUV disk images. A two-limit scheme determines which image's data will occupy the final map. Both limits are set in terms of $\mu = \cos\theta$, where θ is the angle from the disk center. The first limit (designated $\mu_{\rm lim\_merge}$ in the procedure) defines what is considered *good* data for use in merging overlapping regions. For the data presented in this paper, we set $\mu_{\rm lim\_merge} = 0.25882$, which corresponds to $\theta = 75°$. The second limit ($\mu_{\rm lim}$) defines what is considered *good enough* data outside of overlapping regions to merge with (here we set $\mu_{\rm lim} = 0.1$, or $\theta = 84°$). This allows data to be extended close to the poles, while retaining better data for most of the map area. EUV image data that falls outside the outer $\mu_{\rm lim}$ value is masked out immediately; the rest of the data is either *good enough* (it falls only within the $\mu_{\rm lim}$ value), or *good* (it also falls within the $\mu_{\rm lim\_merge}$ value). A pixel-by-pixel algorithm first determines whether the synoptic frame pixel already contains data; if not, the EUV image data is used. If there is already data present in the synoptic frame pixel, the new data is merged (by taking the pixel with minimum intensity) if it has as high a μ value or better than the preexisting data. In this way, the full Sun map is populated with the data that is most reliable and lowest in intensity, emphasizing CHs. This sequence is repeated for each EUV image to build up the final map. A visual representation of the steps of the algorithm is shown in Figure 2.

The MIDM method relies upon using many EUV images of the Sun to generate a full Sun EUV map. This is not a challenge for the *ideal* case of simulations (Section 3), where any observation at any angle and any instant can be modeled. However, with remote sensing, where we lack complete concurrent coverage of the Sun, we must use time-varying images. The resulting CH extents then become a convolution of spatial and temporal information, which are not easily separated (as discussed in Section 4).

We note that this method of merging maps is *designed specifically to highlight dark structures*, with the aim of enhanced CH detection. For other use cases, a minimum μ merge condition could be better. Furthermore, the method does introduce some areas where *good* and *good enough* data are merged. The algorithm could be modified to only keep *good* data where both *good* and *good enough* data are present. However, since near-limb LOS observations are desired to better detect obscured CHs, we allow the two data qualities to merge.

3. MIDM Applied to MHD Model Results

To test the ability of the MIDM method to decrease CH obscuration we utilize our thermodynamic MHD model of the solar corona called Magnetohydrodynamic Algorithm outside a Sphere (MAS; Lionello et al. 2009; Mikić et al. 2018; Török et al. 2018).[1] Here, we use the same MHD solution used in Linker et al. (2021); details about the model calculation are provided in the Appendix of that paper. The corona is integrated to a quasi-steady state using a map of the radial magnetic field at the surface, $B_r^\odot$, as the lower boundary condition, which is based on synoptic map data from the Helioseismic and Magnetic Imager (HMI; Scherrer et al. 2012). The boundary map is processed with data interpolation, smoothing, and filling missing polar data with generated data containing parasitic polarities, all while preserving the flux balance of the map. This processing is described in more detail in Caplan et al. (2019) and follows similar applications of this MHD model and related studies (e.g., Mikić et al. 2018; Boe et al. 2021). The processed radial magnetic map at the model

[1] For more information the MAS model, please visit http://www.predsci.com/mas.

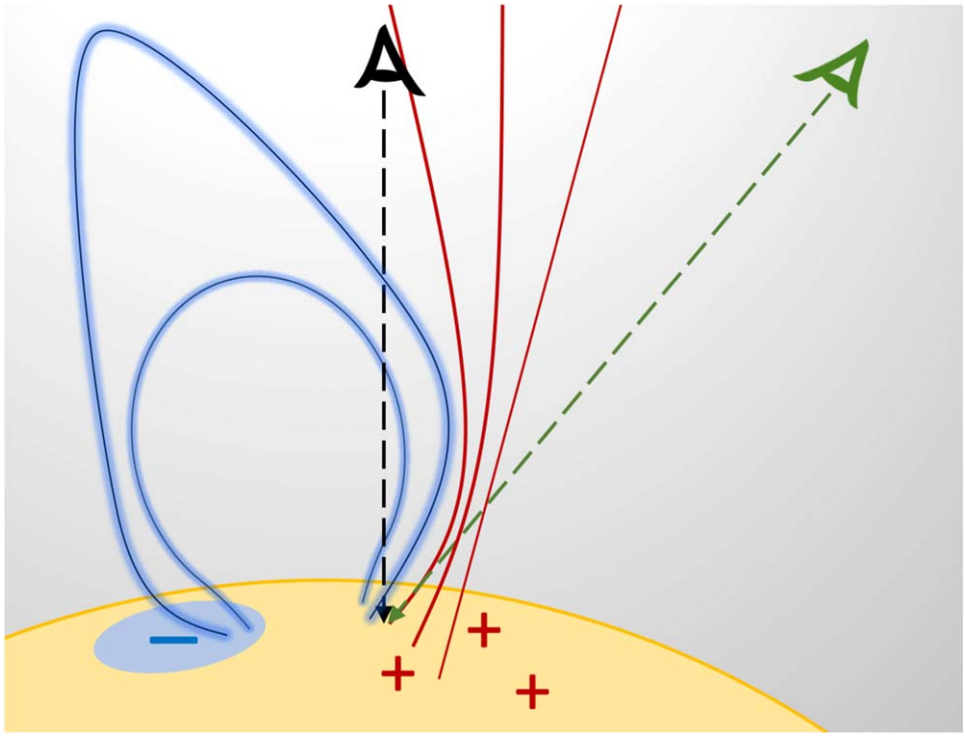

Figure 1. Illustration of CH obscuration. A set of closed loops (blue), with correspondingly high emission, are located adjacent to lower-emission open field (red). The open/closed boundary is obscured for one observer's LOS (black-dashed line) but is visible from another observer's LOS (green-dashed line).

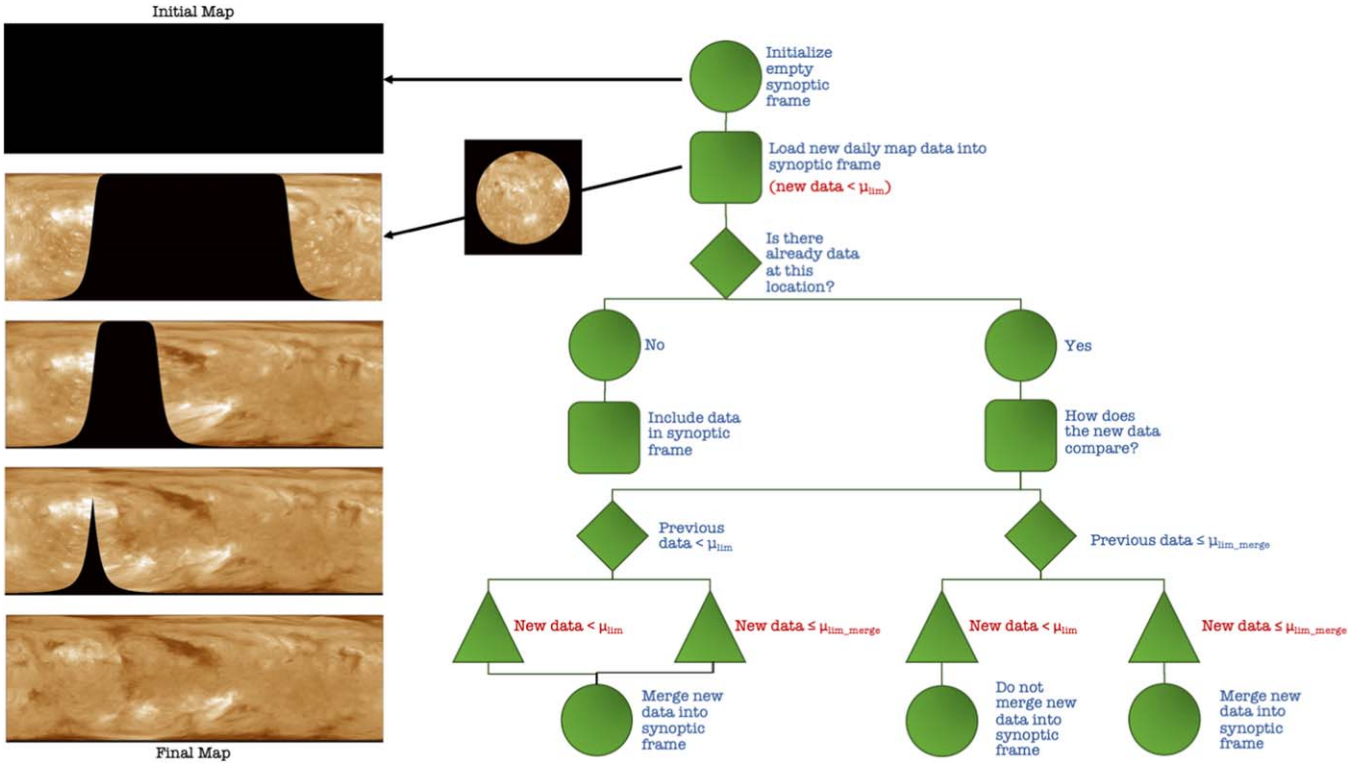

Figure 2. Schematic of the MIDM method for merging EUV images into a full Sun map on a pixel-by-pixel basis. New data take priority, unless its μ value (a measure of data quality) is lower than the data already present. When two pixels are merged, the minimum intensity of the two is used.

resolution (288 × 326 points in latitude/longitude) is shown in Figure 3.

As in Mikić et al. (2018), we use the 3D coronal simulation MHD quantities (i.e., density, temperature) to generate emissivity, and then integrate this quantity along the LOS to forward model SDO/AIA 193A images (AIA; Lemen et al. 2011; Pesnell et al. 2012). Using this method, we generate 111 synthetic emission images at 4° intervals in Carrington longitude with the average B0 angle of SDO during CR 2101 (2010 September 5 to 2010 October 3). These synthetic

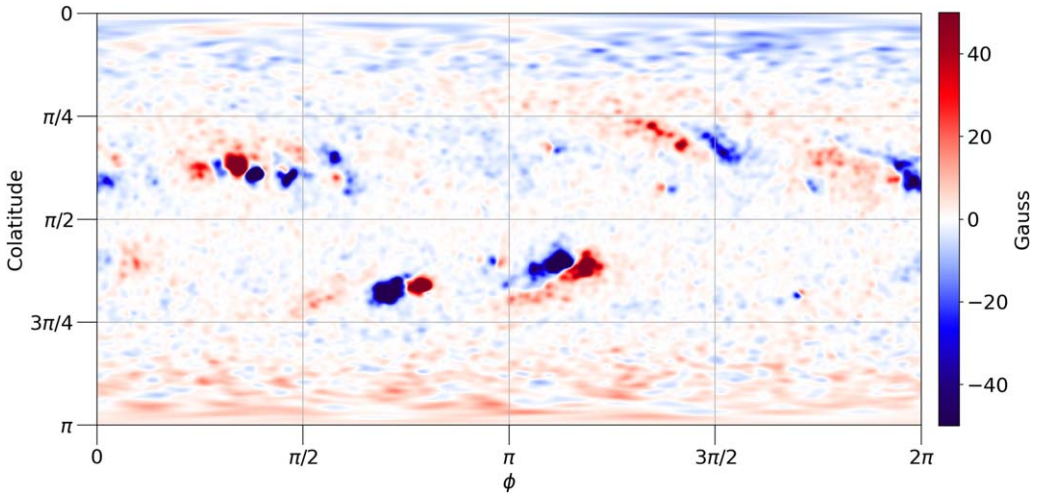

Figure 3. Processed CR 2101 photospheric radial magnetic field map used for the MAS MHD model.

emission images are then processed with a limb-brightening correction technique (described in detail in Caplan et al. 2016). This step is of central importance; in EUV, the limb appears brighter due to the increased LOS through optically thin plasma, which can bias CH detection schemes. The method used is a function of time-averaged intensity values and the angle from disk center.

We generate full Sun synthetic emission EUV maps from the images using both MIDM (described above) and a synoptic map method. The synoptic method uses a Gaussian assimilation FWHM of 2°, similar to the way solar magnetic Carrington maps are built up over a rotation. We extract CHs from both maps using a dual-threshold detection algorithm called `ezseg`. This detection method starts with applying an intensity threshold to the image that is qualitatively determined to be almost guaranteed within CHs (`thresh1`), and then grows the detection from the seed threshold regions to a second threshold chosen to correspond to typical quiet Sun intensities (`thresh2`). Both our limb-brightening correction method and `ezseg` are described in Caplan et al. (2016).[2] We are also developing an improved open-source version of this pipeline, named CHMAP,[3] which incorporates the Caplan et al. (2016) corrections, `ezseg`, MIDM, and additional mapping techniques.

The `ezseg` algorithm has only two tunable parameters (the image intensity threshold values described above). We perform multiple CH detections over a range of parameter values that result in qualitatively reasonable detections. In this case, `thresh1` values are chosen equidistantly at increments of 0.05 between the values 1.2 and 1.4 and `thresh2` values are chosen in the same manner between each `thresh1` value and 1.7. This results in a set of CH maps referred to hereafter as an ensemble. We selected one map from the ensemble that subjectively appears to visually best capture the CHs, with minimal over- or undershoot (yielding unique *best* `ezseg` parameters per EUV map). In Figure 4, we display these *best* cases out of the ensembles from both the full Sun EUV maps made with the synoptic method (in the left column), and from the EUV maps made using the MIDM method (on the right).

[2] Both the limb-brightening correction and `ezseg` source code are available at https://www.predsci.com/chd.

[3] An early release of CHMAP is currently available at github.com/predsci/CHMAP.

It is evident from comparing the boundaries in the top row of Figure 4 that the MIDM map generally has more dark regions, primarily near the poles and some active regions, where the viewing geometry leads to obscuration of the dark regions by intervening structures. To compute open flux estimates, we overlay the CHs on the B_r magnetogram used in the model. The open flux B_r maps are shown in the middle row of Figure 4; it is apparent that the MIDM map on the right captures more of the polar CH open flux due to the suppression of obscuration at very high latitudes. The bottom row of the figure shows the open flux captured by each CH segment (as a percentage of the total open flux) identified with the respective method.

A great advantage of using an MHD model is that the model's open field can be easily computed by tracing field lines through the coronal solution. This allows us to compare the areas and fluxes computed with the EUV-derived CHs to those of the known simulated open field. These open field areas and their percentage flux per region are shown in Figure 5. In the top row, we can see that the open field areas are smaller but with more structure. Also, several small areas are not detected at all in the synthetic emission EUV maps of Figure 4.

3.1. Effective Height Considerations

The open field regions derived from the model's magnetic field differ from those obtained via the CH detection algorithm applied to the synthetic emission images. This effect can be seen by comparing the maps between Figures 4 and 5, and it is due in part to the derivation of the EUV images from a 3D integration into the low corona, yielding an image that has an *effective height* somewhat above the solar surface. In Figure 5, we plot the open field of the model at different heights (at $r = 1.00\,R_\odot$, $1.01\,R_\odot$, and $1.02\,R_\odot$). The open field contour at $r = 1.02\,R_\odot$ best matches the CHs derived from the EUV maps in Figure 6. The open field map at the surface contains the signatures of every tiny patch of parasitic polarity (small-scale polarity of opposite sign) present in the B_r map, while the maps taken slightly higher capture less of this superfine detail.

There are several reasons for this. First, the base of the corona must form above the chromosphere and transition region once the density falloff is sufficient for plasma to heat up to coronal temperatures. For the quiet corona, this generally begins around a height of $1.01\,R_\odot$ (e.g., Figure 18 of Caplan et al. 2016; also Fludra et al. 1999; Giménez de Castro et al.

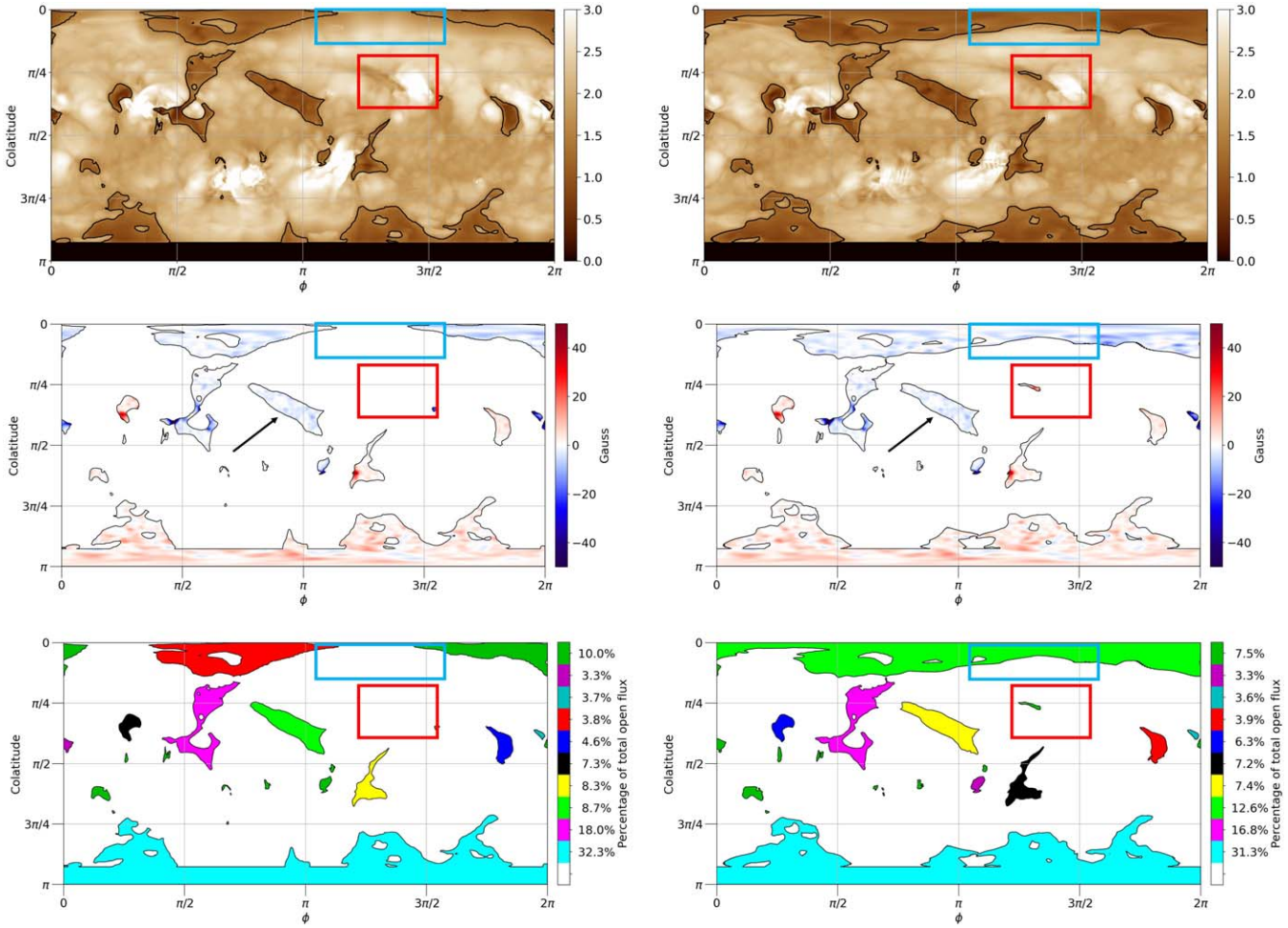

Figure 4. Results of CH detection on the model's synthetic EUV images. The left column shows the subjectively determined *best* visual CH boundaries made with `ezseg` for the synoptic method EUV full Sun map overlaid as the black boundary in each row, while the boundary on the right column uses the MIDM EUV map. The first row shows a composite 193 Å map for each of the respective methods; the second row shows a map of $B_r^{\odot}$ in the model, masked with the respective CH detection contours; the third row shows the percentages of the total open flux in each discrete CH that was detected. The blue rectangles highlight differences in the obscuration of the polar CH between the two methods for all three sets of plots, while the red rectangles show differences in the vicinity of an active region. The black arrow in the middle row indicates the CH whose open flux is computed in Figure 6. The quantitative measurements of total open flux are shown in Figure 6.

2007). In the MAS model, this height is slightly higher, $\sim 1.02\,R_{\odot}$, due to the necessity of broadening the transition region to resolve thermal conduction length scales in the global thermodynamic MHD calculation (Lionello et al. 2009; Mikić et al. 2013; Johnston et al. 2021).

Additionally, because of the rapidity with which the magnetic field drops off with height, the very small parasitic polarities that are apparent on photospheric $B_r$maps will decay quickly, as will their corresponding closed arcade. This will naturally lead to short loops that are unlikely to reach coronal temperatures and densities under quiescent conditions and may not appear as bright structures in remote sensing data. Therefore, coronal EUV observations show the more uniform CHs which are reproduced by the slightly higher effective height in the simulations.

Moreover, as discussed in Section 5.3 of Linker et al. (2021), projecting detected CH boundaries down onto the photosphere overestimates the flux due to the expansion of the open field with height. If a significant amount of the EUV emission in the wavelength being used for detections originates from a larger height, the expansion of the magnetic field must be taken into account to avoid overestimation. The results shown in the subsequent sections here support this effective height consideration. Therefore, we consider the model's effective EUV height to be $R_{\odot} = 1.02$ for the remainder of this paper.

3.2. Open Flux Results

The open flux results for the equatorial CH which crosses the $\phi = \pi$ line in the northern hemisphere are shown in the left panel of Figure 6. The plot on the left shows the open flux calculations and area for the single equatorial CH discussed above, while the plot on the right shows these quantities for the full simulation map. The green and red triangles show the model's known open flux (hereafter referred to as the true open flux), based upon the various combinations of the open field and magnetic field maps taken at $r = 1.00$ and $1.02\,R_{\odot}$. This serves to illustrate the importance of using the correct effective height, and to give context to the results of the CH detections using the range of thresholds discussed in Section 3. The black circles are the results of the CH detections using the model-derived synoptic EUV map, while the blue squares are the analogous results using the EUV map made with the MIDM algorithm. The filled circle and square represent the set of CH detection threshold values that were considered to provide the *best* agreement with visual inspection; as can be seen in the

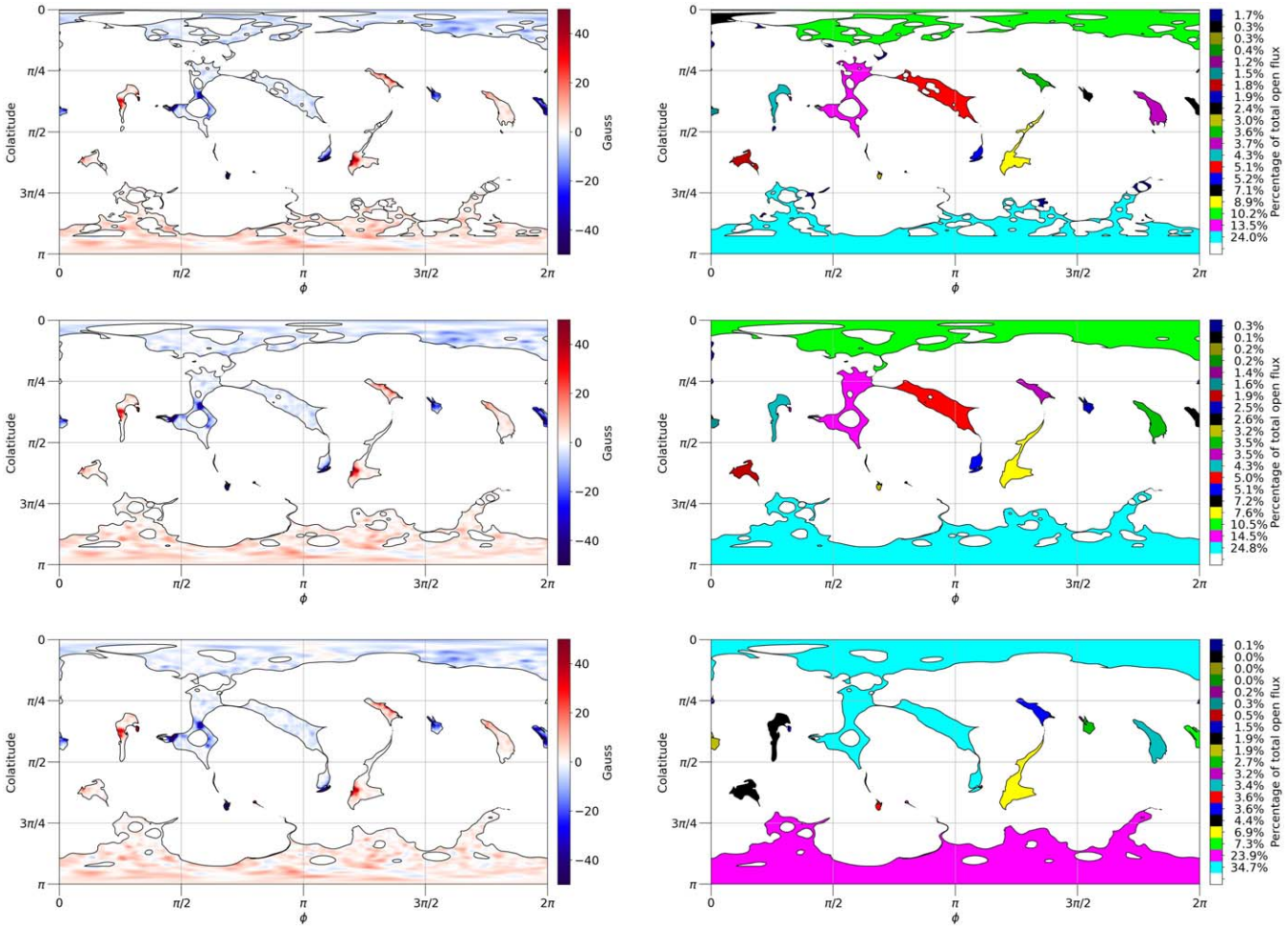

Figure 5. Top to bottom: open field maps from the MHD model at $r = 1.00\,R_\odot$, $1.01\,R_\odot$, *and* $1.02\,R_\odot$, respectively. These can be compared with the middle panels of Figure 4. The left column shows the B_r magnetogram; the right column shows the relative percentages of open flux.

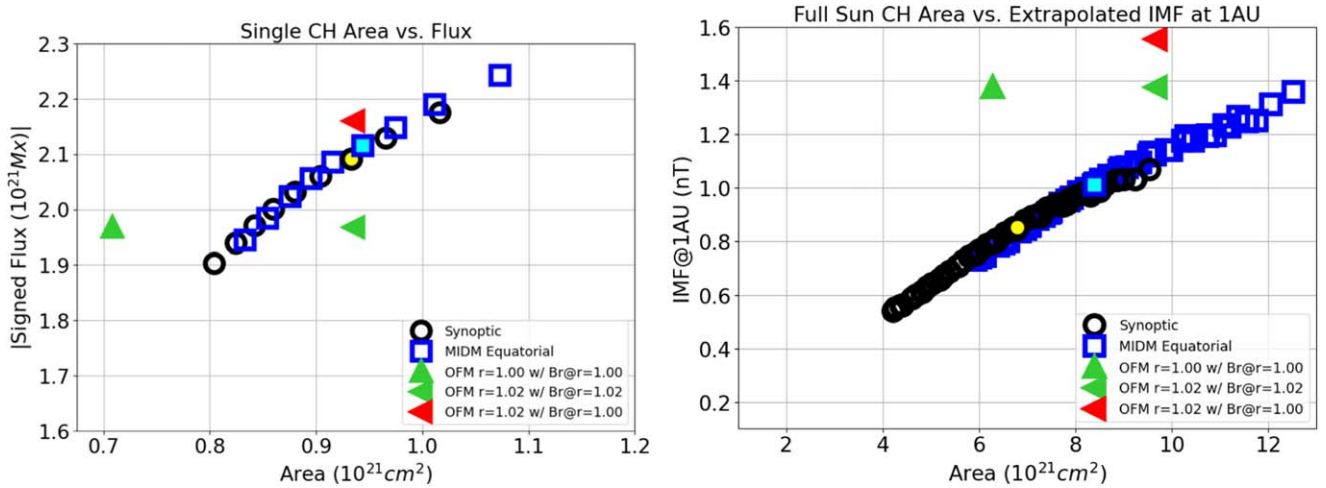

Figure 6. Model results. Left: CH area vs. open flux measurements for the equatorial CH indicated by the black arrow in Figure 4. Right: CH area vs. extrapolated interplanetary magnetic field at 1 au, for the full Sun. In each plot, the blue squares and black circles are the results of overlaying the CH detections on the surface B_r magnetogram for the full ensemble of reasonable CH detections using the MIDM and synoptic EUV maps, respectively. The yellow-filled circle and the cyan-filled square are the selected best visual CH detections within each ensemble. The triangles represent the open flux computed with the true open field contour at various effective heights (see Section 3.1). The green triangles use B_r at the same height as the known open field contour, while the red triangles use (incorrectly) the surface B_r at the non-surface open field contour height.

figure, both of the filled shapes correspond quite well to the model's *true* areas derived with the effective height of $r = 1.02\,R_\odot$. We see that, for the single CH, the results from the synoptic and MIDM EUV maps are similar. This is expected, as there are no bright regions near the CH, and it is centrally located on the disk, thus minimizing the potential for

obscuration along the LOS that may plague observations at more oblique angles or that have large, neighboring active regions.

In each plot, the known model open flux is shown as green triangles. The two orientations of the triangles indicate different radii at which the open flux integral is taken (▲ $\rightarrow r = 1.00\,R_\odot$, ◀ $\rightarrow r = 1.02\,R_\odot$), using the corresponding B_r magnetic data at each radius. As the radius increases, the open flux remains the same, but the area of the open field map increases due to magnetic field expansion, as expected. The true open field area at the solar surface is shown to be smaller than almost all CH detections, and the true open flux is lower than both methods' *best* detections. However, the open field area for higher surface heights starts to match the CH areas, while the open flux remains the same.

Along these lines, we investigated a potential contributing factor to the open flux problem, the discrepancy between the effective height of EUV-derived CH detections and the B_r map. B_r is taken at $r = 1.00\,R_\odot$ in both simulations and observations, while the CH detections in the model are better approximated with a height of $r = 1.02\,R_\odot$. To see the effect of this mismatch, we computed the open flux using the model's open field at $r = 1.02\,R_\odot$ incorrectly combined with the B_r map at $r = 1.00\,R_\odot$ (as is done when using observed CH maps). Shown as the red left triangle, both the area and open flux now very closely match the CH-derived results, with the CH measuring a slightly lower open flux. This implies that utilizing a photospheric magnetic field paired with EUV CH detections may yield open flux estimates that are actually somewhat higher than the true open flux. We note, however, that this effect may be smaller in real observations due to a lower EUV effective height, and these measurements are for a central, relatively unobscured CH. As will be discussed shortly, the situation changes when considering the full Sun.

In the right panel of Figure 6, we show the analogous calculation for the full Sun. Here, we represent the open flux as an extrapolated interplanetary magnetic field at 1 au (Linker et al. 2017). In order to properly compare all results, we limit the open field maps in latitude at the southern pole to match the area of missing data in the EUV maps due to the Earth's position precluding observation of the southern pole at this time. This excluded region is shown as the black portion visible along the southernmost extent of the top row of Figure 8. In all cases, we assume the missing polar area is an open field. This effect is small, as the open flux measurements between the full model open field with or without the latitude limit are within 0.1% of each other.

Here we see that the MIDM CH detections have an overall trend to be both higher area and higher open flux than the synoptic detections. This is especially noticeable when comparing the results of the two *best* CH detections for each type (filled cyan square and filled yellow circle). This is likely due to the greater role that obscuration at high latitudes and for smaller patches near bright regions along the LOS may play. However, unlike in the case of the single CH, the true open flux from the model is higher than most reasonable CH detections, even when using MIDM. As noted by Linker et al. (2021), MIDM captured 73.7% of the true open flux in the model (1.01 nT scaled to 1 au for the *best* visual detection, as opposed to the true value of 1.37 nT). Looking at the overlaid maps in Figure 4, one sees that much of this flux could be coming from the small open field areas near bright regions that are not dark in the EUV images, or in regions where the open field is near the intensity of the dark quiet Sun, preventing the detection algorithm from capturing them. We can also see in Figure 6 that calculating the true open flux by overlaying the true open field at $r = 1.02\,R_\odot$ on the surface B_r magnetogram at $r = 1.00\,R_\odot$ (similar to what one can do with observations) increases the value of the open flux estimate as it did in the single CH case. This implies that the open flux estimates using EUV-detected CHs are actually slightly higher than they should be. However, this overestimation of open flux is much smaller than the large underestimation caused by the missing regions. We therefore see that for the full Sun, the MHD model indicates that one is likely to underestimate the open flux when using CH maps overlaid on B_r magnetograms, contributing to the observational open flux problem.

We point out that there were several *reasonable-by-eye* detections using the MIDM method that result in correct open flux values, but none using the synoptic method. However, the contours yielding the correct open flux have larger CH areas than the true open field map.

4. MIDM Applied to SDO Observations

In this section, we apply the MIDM procedure to SDO observations taken during CR 2101 and conduct similar open flux calculations using SDO HMI data. We compute flux estimates using a pole-filled HMI synoptic map data series for CR 2101 (from the `hmi.synoptic_mr_polfil_720s` data series at the SDO JSOC). The map is used at full resolution with no modifications, instead of the smoothed map used in the model. This is because observational CH detections can be made at high resolution, and it is desirable to use consistent resolution between the magnetic and EUV data. The B_r map used is shown in Figure 7.

We selected 111 SDO/AIA 193 Å EUV images at 6 hr cadence, centered in time within CR 2101. They were then processed with our limb-brightening correction method. The EUV images were combined into EUV maps using both the synoptic and MIDM methods in the same manner as described in Sections 2 and 3. Using the CH detection algorithm `ezseg`, we extracted a *reasonable* ensemble of CH detections from both the MIDM and Synoptic EUV maps, and again chose the subjectively *best* visual detection of each to highlight. These detections are shown in Figure 8.

Here the maps derived from the two methods differ more obviously than in the model case. One reason for this is the fact that the surface structures, including the CHs, are evolving over the CR. The MIDM method thus *washes out* fine details, much more than the synoptic method, which has a much narrower data assimilation window. At this cadence, transient changes like individual jet eruptions or flares are likely to vanish, but the large-scale maximal extent of the visible CH boundaries will be captured.

The middle panels of Figure 8 compare the open field captured using the CH detections from the traditional synoptic (left) and MIDM (right) methods. The cyan box highlights the MIDM method's improved polar CH boundary due to the improved coverage provided by many different LOS viewing perspectives, just like the simulated version. The red box indicates a small low-latitude CH that is detected using MIDM and not captured at all in the synoptic map. This difference is clearer than the region highlighted in red from Figure 8, which also indicated differences in open flux near active regions. The algorithm's emphasis on

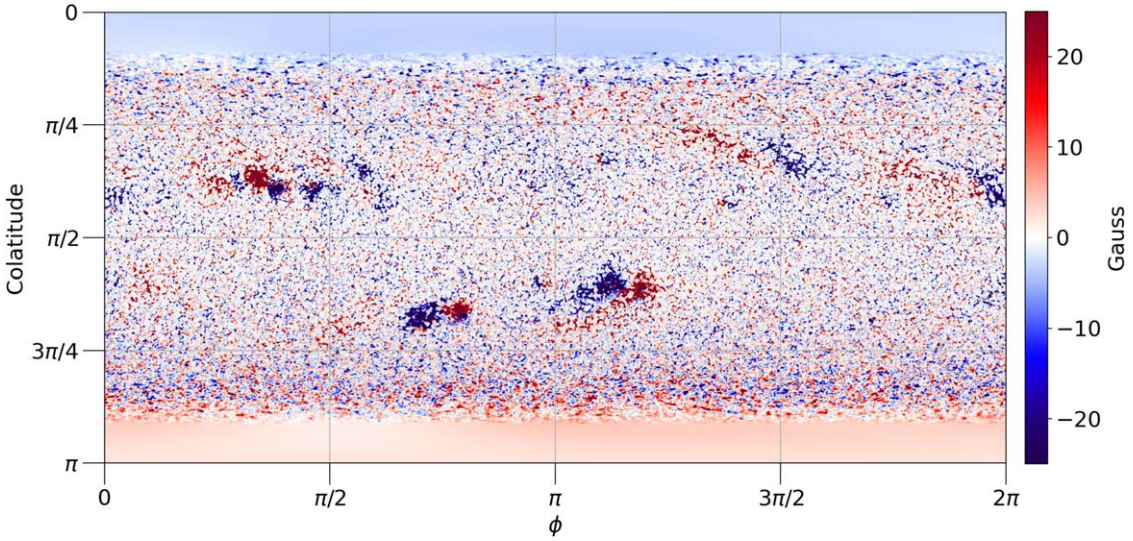

Figure 7. Pole-filled HMI B_r map used with AIA observational data for open flux calculations.

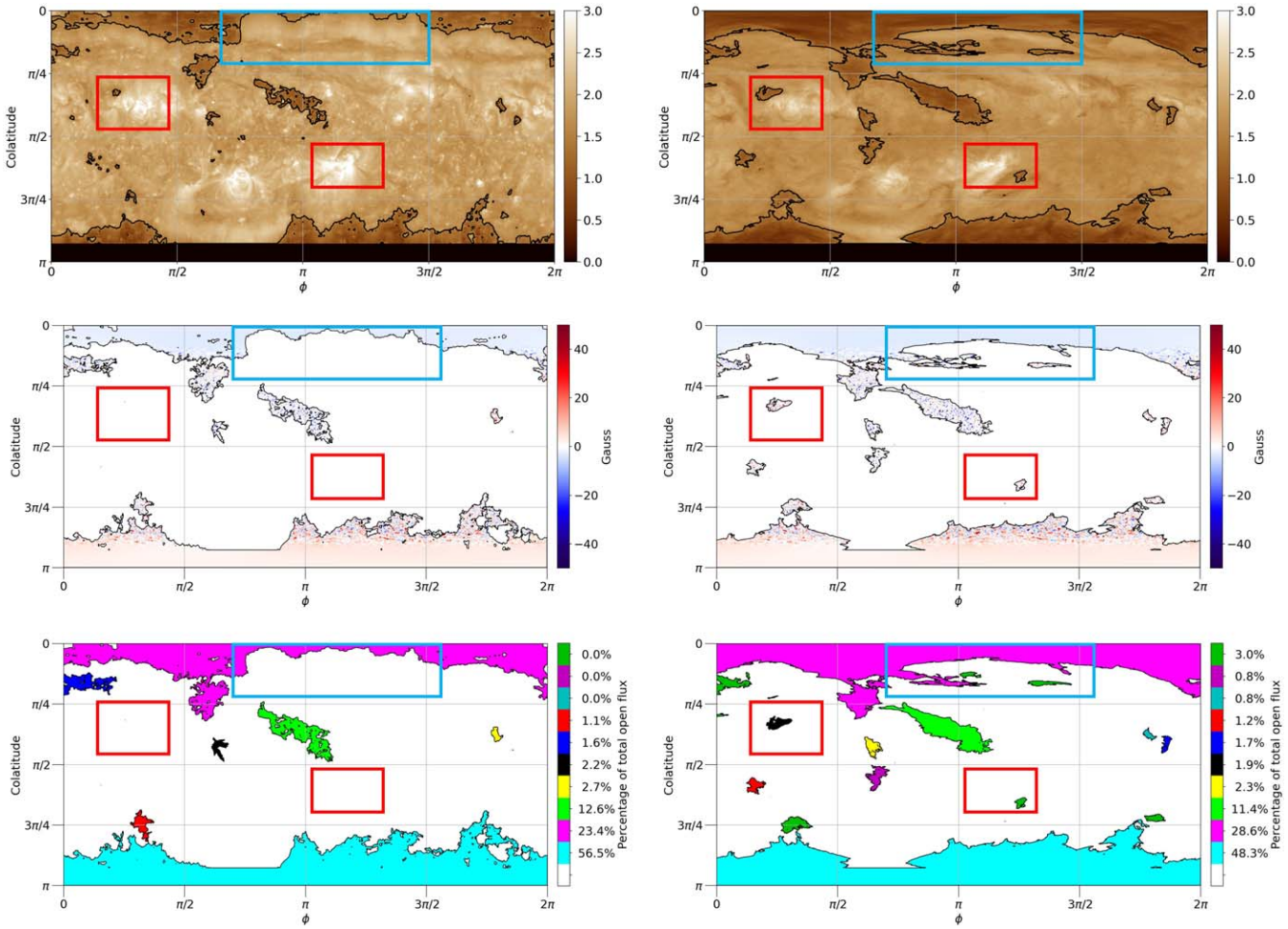

Figure 8. Figure analogous to Figure 4 but for AIA data, with a cyan box highlighting differences along the polar CH boundary and the red box indicating differences in the vicinity of an active region.

high-quality minimum-intensity data prioritizes data from CHs when they are observed most distinctly.

The bottom two panels of Figure 8 show the percentage of open flux within each CH on the map for the synoptic and MIDM EUV maps, respectively. In this case, we only have B_r data at the solar surface, even though the EUV data is at an effective height of $r \approx 1.01\,R_\odot$ (Caplan et al. 2016). Since the effective height for the EUV data is lower than the EUV effective height of the model, we expect the effect of the height mismatch to be less than in the model case.

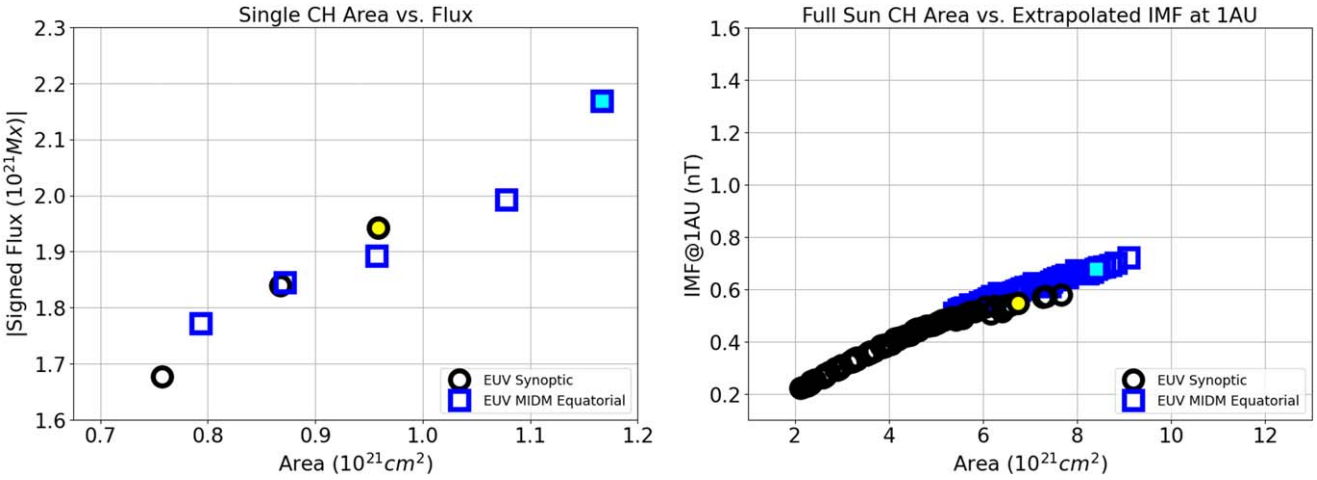

Figure 9. Observational open flux results. Left: CH area vs. open flux measurements for the equatorial CH which crosses the $\phi = \pi$ line. Right: CH area vs. extrapolated interplanetary magnetic field at 1 au, for the full Sun. The interplanetary flux inferred from observations for this time period was ≈1.71 nT (Linker et al. 2021).

The open flux results for the central equatorial CH are shown in the left panel of Figure 9. Similar to the model case, the yellow-filled circle and the cyan-filled square represent the subjective *best* visual CH detections. Here we see a much wider spread of areas and fluxes when varying CH detection parameters than we did in the model results. In contrast to the model case, however, the MIDM for the central CH generally yields larger areas and fluxes than the synoptic case. This is likely due to the evolution of the CH as it rotates through the data; while the CH does not grow noticeably during the period of observation, the algorithm ensures that dark regions are prioritized if the view is reasonable. This naturally finds the maximal extent of the boundary in the case of evolution, and minimizes the role of transient brightenings that may shrink or distort the boundary in a single instantaneous image.

For full Sun results (the right panel of Figure 9), we set the same southern pole latitude limit as in the model case. While the areas and open flux for the single central CH are similar to those in the MHD model case, the full Sun areas are lower and the full Sun open flux values are much lower. The MIDM method once again generally exhibits greater CH areas, and larger open fluxes than the synoptic method for most CH detections. However, the full Sun open flux scaled to 1 au was still very low (consistent with the open flux problem): 0.68 nT, compared to 1.71 nT inferred from interplanetary observations (Linker et al. 2021).

5. Discussion

Several key points emerge from the above analyses:

1. MIDM effectively captures more CH area than traditional synoptic methods do. The MIDM results are generally both higher area and higher derived open flux than the synoptic results, including the two subjectively *best-looking* CH detections. This is due to the algorithm's ability to minimize the obscuration of dark features by intervening bright structures as it includes all available LOSs. While part of this increase may also be due to CH evolution, the model results (which had no evolution) imply that a significant amount of this increase is due to the MIDM observing CH regions that are otherwise obscured. Of course, CH evolution is a consideration when using the MIDM method on observational data. Since the MIDM builds up the EUV map from several full EUV images, large changes in CH morphology are effectively cumulative and may result in CH detections being too large. Our presented case used EUV images spanning a full Carrington rotation. To minimize this problem, images from other instruments in orbit around the Sun could be used (such as the STEREO spacecraft), or the map could be built using data from less time (a running window could be used to still achieve a full Sun EUV map). We also note that the MIDM method has two tunable parameters (the view angle limits of *good* and *good enough* data) that can be used to optimize the method for various applications. Lastly, active regions are one of the main causes of obscuration, so a scaling factor to expand the CH in their vicinity could be implemented to improve detections. This will be investigated in future adjustments to the algorithm.
2. The MHD model's true full Sun open flux remains higher than that derived from most of the CH detections, even when using MIDM. For the best visual detection, the true open flux of the model (1.37 nT scaled to 1 au) was 35.6% higher than the detected flux (1.01 nT). There are several factors that may contribute to this. The first is the role of *bright* open flux. From investigating the overlaid maps in Figure 6, it is apparent that much of this flux comes from the small open field areas near active regions. These are not dark in the EUV images, or in regions where the open field is near the intensity of the dark quiet Sun, preventing the detection algorithm from capturing them. Another factor to consider is the respective resolutions and effective heights of the EUV and solar surface B_r data when using them to estimate open flux. As we saw in the model results, the morphology for the open field is noticeably smoothed out even at small values above the surface. When masking the true open field on the surface magnetogram with the detected CHs, the resultant open field areas and open fluxes are inaccurate. Although the effect of this is harder to gauge observationally, where the actual open flux values are unknown, it should be considered a complicating factor when

combining CH and magnetic data. We discuss in the next section some possible steps to mitigate this challenge for future work.

3. The disparity between the detected open flux from CHs and the inferred interplanetary flux is far greater for the observations than in the detection test with the model. The open flux inferred from interplanetary observations (1.71 nT) was 2.5 times greater than the open flux detected with MIDM (0.68 nT). The under-detection of open flux in the model test may give us clues as to the source of some of the missing flux, where we found that there were small equatorial open field regions that did not appear dark in the synthetic EUV observations, yet contributed a nontrivial amount of the open flux. If these small under-sampled regions are even more prevalent on the Sun than in the model, they could contribute substantially to the open flux, although they are unlikely to fully resolve the open flux problem.

6. Conclusions

We have introduced the MIDM method for constructing full Sun EUV maps as an alternative to the traditional synoptic approach. The primary function of the MIDM approach is to utilize multiple vantage point image sequences to identify the existence of dark patches on the solar disk. When using a thermodynamic MHD model, the MIDM method was shown to better match EUV CH detections with the true distribution of open field in the model. It was most helpful near the poles and in areas where CHs were adjacent to bright active regions.

When applying MIDM to SDO/AIA observations, we detected some new regions and generally larger CHs compared to traditional synoptic maps, yielding higher overall open flux estimates. However, the flux estimates were still very low overall. We observed that in the MHD model, there were numerous small equatorial open field areas that contributed a large percentage of the total open flux. These areas, associated with active regions, were difficult to detect in the synthetic EUV images as CHs (and in some cases, they were not detected at all). Such areas could help explain why the open flux in the observations are low, and account for some portion of the missing open flux described in the open flux problem.

We have also demonstrated how the effective height of EUV images can have a nontrivial effect on open flux estimations using surface magnetic field data. A more accurate estimation of open flux may in fact be slightly lower than those derived from photospheric magnetograms. One way to combat the effective height problem with future work would be to use the B_r of a high-resolution potential field model to extrapolate the magnetic field values at a height matching the effective height of the EUV data. This is a very feasible alteration that could quantitatively improve our current estimate methods.

The core assumptions that MIDM is built around (particularly the emphasis on selecting minimum-intensity pixels) differ from those underlying traditional synoptic mapping, and our results show the major impacts of those assumptions. The study of CH boundaries, slow solar wind formation, and interchange reconnection all depend, at least in part, upon accurately identifying the open/closed boundary and probing the magnetic field there. Challenges with obscuration have been a consistent problem with CH studies; MIDM can help address this problem by extrapolating the maximal CH area detected through multi-point observations. On the other hand, in producing larger CHs from data at an optimal viewing angle, MIDM does introduce a time convolution to the resultant map that is more complex than the simple dependence of time with longitude in traditional synoptic maps.

Despite the improvements in open flux detection provided by MIDM, the detection still underestimated the open flux in the model (capturing only 73.7% of the flux). The source of much of this discrepancy was small open field regions near active regions. For the observed case, the inferred interplanetary flux was 2.5 times greater than the solar open flux provided by the MIDM detection. For this solar minimum time period, it is unlikely that detection issues alone could account for the missing open flux, but they may be a significant component. Near solar maximum, there are many active regions that obscure equatorial CHs, and so under-detection of open flux is likely to be even more prominent. MIDM may help to mitigate these effects by detecting more of the slivers of open flux near bright loop footprints.

Acknowledgments

This work was supported by the NASA Heliophysics Supporting Research (grant 80NSSC18K1129) and Guest Investigator programs (grants NNX17AB78G and 80NSSC19K0273), the NSF PREEVENTS program (grant ICER1854790), and the STEREO SECCHI contract to NRL (under subcontract N00173-19-C-2003 to PSI). We acknowledge valuable collaborations with the International Space Science Institute (ISSI) team "Magnetic open flux and solar wind structuring in interplanetary space" (2019–2022).

ORCID iDs

Ronald M. Caplan https://orcid.org/0000-0002-2633-4290
Emily I. Mason https://orcid.org/0000-0002-8767-7182
Cooper Downs https://orcid.org/0000-0003-1759-4354
Jon A. Linker https://orcid.org/0000-0003-1662-3328

References

Altschuler, M. D., Trotter, D. E., & Orrall, F. Q. 1972, SoPh, 26, 354
Antiochos, S. K., Mikić, Z., Titov, V. S., Lionello, R., & Linker, J. A. 2011, ApJ, 731, 112
Boe, B., Habbal, S., Downs, C., & Druckmüller, M. 2021, ApJ, 912, 44
Bohlin, J. D. 1977, in Coronal Holes and High Speed Wind Streams, ed. J. B. Zirker (Boulder: Colorado Associated Univ. Press), 27
Boucheron, L. E., Valluri, M., & McAteer, R. T. J. 2016, SoPh, 291, 2353
Caplan, R. M., Downs, C., & Linker, J. 2019, American Geophysical Union, Fall Meeting, 2019, SH43E–3389
Caplan, R. M., Downs, C., & Linker, J. A. 2016, ApJ, 823, 53
Cranmer, S. R., van Ballegooijen, A. A., & Edgar, R. J. 2007, ApJ, 171, 520
Crooker, N. U., Gosling, J. T., & Kahler, S. W. 2002, JGRA, 107, 1028
DeForest, C. E. 2004, SoPh, 219, 3
Downs, C., Linker, J. A., Mikić, Z., et al. 2013, Sci, 340, 1196
Downs, C., Roussev, I. I., van der Holst, B., et al. 2010, ApJ, 712, 1219
Downs, C., Warmuth, A., Long, D. M., et al. 2021, ApJ, 911, 118
Fisk, L. A., Schwadron, N. A., & Zurbuchen, T. H. 1998, SSRv, 86, 51
Fludra, A., Del Zanna, G., Alexander, D., & Bromage, B. J. I. 1999, JGR, 104, 9709
Garton, T. M., Gallagher, P. T., & Murray, S. A. 2018, JSWSC, 8, A02
Gibson, S. E., Kucera, T. A., Rastawicki, D., et al. 2010, ApJ, 724, 1133
Giménez de Castro, C. G., Varela Saraiva, A. C., Costa, J. E. R., & Selhorst, C. L. 2007, A&A, 476, 369
Harvey, J. W., & Sheeley, N. R. 1977, SoPh, 54, 343
Heinemann, S. G., Temmer, M., Heinemann, N., et al. 2019, SoPh, 294, 144
Henney, C. J., & Harvey, J. W. 2005, in ASP Conf. Ser. 346, Large-scale Structures and Their Role in Solar Activity, ed. K. Sankarasubramanian, M. Penn, & A. Pevtsov (San Francisco, CA: ASP), 261

Johnston, C. D., Hood, A. W., De Moortel, I., Pagano, P., & Howson, T. A. 2021, A&A, 654, A2
Kaiser, M. L. 2005, AdSpR, 36, 1483
Kirk, M. S., Pesnell, W. D., Young, C. A., & Hess Webber, S. A. 2009, SoPh, 257, 99
Krieger, A. S., Timothy, A. F., & Roelof, E. C. 1973, SoPh, 29, 505
Krista, L. D., & Gallagher, P. T. 2009, SoPh, 256, 87
Lemen, J. R., Title, A. M., Akin, D. J., et al. 2011, SoPh, 275, 17
Linker, J. A., Caplan, R. M., Downs, C., et al. 2017, ApJ, 848, 70
Linker, J. A., Heinemann, S. G., Temmer, M., et al. 2021, ApJ, 918, 21
Lionello, R., Linker, J. A., & Mikić, Z. 2009, ApJ, 690, 902
Lowder, C., Qiu, J., & Leamon, R. 2017, SoPh, 292, 18
Lowder, C., Qiu, J., Leamon, R., & Liu, Y. 2014, ApJ, 783, 142
Mason, E. I., & Uritsky, V. M. 2022, ApJL, 937, L19
Mikić, Z., Downs, C., Linker, J. A., et al. 2018, NatAs, 2, 913
Mikić, Z., Lionello, R., Mok, Y., Linker, J. A., & Winebarger, A. R. 2013, ApJ, 773, 94
Müller, D., St. Cyr, O. C., Zouganelis, I., et al. 2020, A&A, 642, A1
Neupert, W. M., & Pizzo, V. 1974, JGR, 79, 3701
Pesnell, W. D., Thompson, B. J., & Chamberlin, P. C. 2012, SoPh, 275, 3
Reiss, M. A., Muglach, K., Möstl, C., et al. 2021, ApJ, 913, 28
Riley, P., Ben-Nun, M., Linker, J. A., et al. 2014, SoPh, 289, 769
Rotter, T., Veronig, A. M., Temmer, M., & Vršnak, B. 2012, SoPh, 281, 793
Scherrer, P. H., Schou, J., Bush, R. I., et al. 2012, SoPh, 275, 207
Scholl, I. F., & Habbal, S. R. 2008, SoPh, 248, 425
Schwadron, N. A., Fisk, L. A., & Zurbuchen, T. H. 1999, ApJ, 521, 859
Sheeley, N. R. J., Harvey, J. W., & Feldman, W. C. 1976, SoPh, 49, 271
Török, T., Downs, C., Linker, J. A., et al. 2018, ApJ, 856, 75
Verbeeck, C., Delouille, V., Mampaey, B., & De Visscher, R. 2014, A&A, 561, A29
Viall, N. M., & Vourlidas, A. 2015, ApJ, 807, 176
Wallace, S., Arge, C. N., Pattichis, M., Hock-Mysliwiec, R. A., & Henney, C. J. 2019, SoPh, 294, 19
Wang, Y.-M., & Sheeley, N. R., Jr. 1990, ApJ, 355, 726